electronics

MDPI

Article

Low-Cost W-Band Dual-Mode SIW Bandpass Filters Using Commercially Available Printed-Circuit-Board Technology

Xiaolong Huang [1,*] and Zheng Liu [2,*]

[1] School of Electronic and Information Engineering, South China University of Technology, Guangzhou 510641, China
[2] Department of Electrical and Computer Engineering, Princeton University, Princeton, NJ 08544, USA
* Correspondence: xlhuang1988@foxmail.com (X.H.); zhengl@alumni.princeton.edu (Z.L.)

Abstract: W-band filters play a crucial role in modern millimeter-wave communication and radar systems, finding applications in 5G/6G networks, automotive radar, and passive imaging. With the growing demand for higher data rates and efficient wireless communication, W-band filter development has gained significant attention in recent years. Various design techniques and fabrication technologies have been explored for improved performance and integration possibilities. This paper presents a planar substrate-integrated waveguide (SIW) dual-mode cavity filter as a solution to the challenges faced by previous designs in terms of integration, size, and cost. The dual-mode cavity coupling principle and design parameters are analyzed to optimize the filter's performance. A W-band 4th-order dual-mode filter prototype is designed and fabricated on a 0.127-mm-thick RO5880 substrate, and a finline waveguide-to-microstrip transition structure is employed for compatibility with the test instrument. Simulation and experimental results demonstrate that the proposed filter exhibits low insertion loss, good in-band standing wave performance, and improved out-of-band suppression. Moreover, a visible high-frequency out-of-band transmission zero is implemented to enhance the steep roll-off characteristics in the high-frequency out-of-band region.

Keywords: dual-mode cavity; millimeter-wave communication; PCB; SIW; W-band filter

Citation: Huang, X.; Liu, Z. Low-Cost W-Band Dual-Mode SIW Bandpass Filters Using Commercially Available Printed-Circuit-Board Technology. *Electronics* **2023**, *12*, 3624. https://doi.org/10.3390/electronics12173624

Academic Editor: Giovanni Andrea Casula

Received: 6 August 2023
Revised: 20 August 2023
Accepted: 26 August 2023
Published: 27 August 2023

1. Introduction

W-band filters are indispensable components in modern millimeter-wave communication and radar systems, playing a critical role in diverse applications such as 5G networks, automotive radars, and passive imaging. With the ever-increasing demand for higher data rates and more efficient wireless communication, the development of W-band filters has garnered significant attention over the past decade. Researchers have explored various design techniques and advanced fabrication technologies in pursuit of improved performance and integration possibilities [1–4].

Notably, some pioneering works, such as those referenced in [1–3], have successfully leveraged 3D print technology to create W-band filters with low-loss characteristics. Additionally, Ref. [4] demonstrated the use of laser micro-machine processing, achieving promising results in terms of low loss. However, one notable limitation of these early designs lies in their 3D structure, posing challenges when attempting to integrate them with planar circuits and chips [5–11].

To address the integration issue, efforts have been made to explore planar-based fabrication techniques. For instance, in [12], a pseudo-elliptical response filter at the W-band was fabricated using thick SU-8 photo-resist technology, which represented an advanced film processing approach. Despite its progress, the total thickness of the filter remained relatively large compared to planar circuits. Similarly, Ref. [13] introduced W-band gap waveguide bandpass filters using the micro-electro-mechanical systems (MEMS) technique, showcasing promising low-loss properties and ease of integration with planar

circuits. However, these filters still exhibited a substantial size, which could be a concern in certain applications. Another approach, involving a silicon-based W-band bandpass filter with a micromachined air-cavity resonator [14], faced similar challenges, emphasizing the importance of compact and efficient filter design.

Addressing the limitations of previous works, Ref. [15] proposed a SIR interdigital W-band bandpass filter based on TSV Technology. Despite its ingenuity, the fractional bandwidth of this filter proved to be impractical for real-world systems. In an attempt to create an on-chip W-band filter with compatibility for active chips, Refs. [16,17] introduced a design based on thin cavities in CMOS processing. However, insertion loss remained an issue due to the low-quality factor of the resonant cavity. While GaAs-based on-chip filters presented higher quality factors [18,19], their reliance on high-mode single-mode SIW cavities meant substantial spatial requirements and cost considerations.

In addition to size-related challenges, on-chip components often come with significant costs. Seeking cost-effectiveness and compatibility with other planar circuits, Ref. [20] proposed a compact planar W-band filter based on EBG Packaging and LTCC processing. Nevertheless, the filter's loss remained a concern. This prompted the development of low-cost W-band SIW bandpass filters using commercially available printed-circuit-board technology [21], which exhibited notable improvements in cost and compatibility. However, the single-mode design still resulted in relatively large filter sizes.

To overcome the limitations of existing approaches and achieve a breakthrough in compact design, Refs. [22,23] introduced the use of a quarter-mode substrate-integrated waveguide cavity. While this approach aimed to miniaturize W-band packaged filtering circuits, the quarter-mode SIW waveguide introduced higher losses compared to full-mode SIW cavities. Ref. [24] introduced an interesting idea to design a W-band SIW filter using the high mode; however, it still lacks experimental verification. Seeking a balance between compact size and performance, Refs. [25–27] explored improved TM dual-mode cavities for W-band filters. Nevertheless, the traditional waveguide used in this method had a large vertical height and limited compatibility with planar circuits.

Given these challenges and the demand for an economical, compact, and low-loss W-band filter, our research proposes a solution in the form of a planar substrate integrated waveguide (SIW) dual-mode cavity. Through harnessing the benefits of planar integration and meticulous design, we strive to lay the foundation for more effective and practical W-band filtering solutions. Based on an investigation of publicly available literature, there is limited use of commercial PCB processes for designing planar substrate integrated waveguide (SIW) filters in W-band. Literature reference [21], which employs the fundamental mode of SIW for filter design, stands as a representative example. As an improvement, our design employs a compact dual-mode cavity. For the first time, we achieved and validated a low-loss SIW dual-mode filter in the W-band using cost-effective commercial PCB processes. In comparison to costly advanced fabrication methods, this approach offers significant cost advantages. Furthermore, due to its potential for direct integration with planar circuits, it holds promising application prospects.

The subsequent sections of this paper are structured as follows: Section 2 delves into the analysis of the coupling principle and design parameters of the dual-mode cavity. Section 3 introduces the design process of the W-band dual-mode filter, including its assembly with transition structures and subsequent verification through measurement. Finally, the conclusion of this article is presented in Section 4.

2. Analysis of Dual Mode SIW Cavities

2.1. Dual-Mode Cavity Coupling Principle

Higher-order modes often accompany degenerate modes, and in most cases, degenerate modes are orthogonal to each other, with no energy exchange. However, when certain perturbations are introduced at appropriate positions, energy coupling between degenerate modes can be achieved. Therefore, in filter design, one can choose to excite only one of these modes to suppress its degenerate mode or fully utilize the degenerate modes to

realize a dual-mode filter. The advantage of exciting only one mode is that the design is simpler and can be carried out following the steps of designing a single-mode filter discussed in the previous chapter. However, compared to dual-mode filters, achieving the same selectivity characteristics would require more cavities, resulting in increased cascade losses and overall larger filter size.

On the other hand, dual-mode filters can make full use of the degenerate modes of the cavity to achieve better selectivity characteristics. Reducing the order directly reduces the number of cavities and minimizes cascade-related losses. However, dual-mode filter design is much more complex due to the coupling issues compared to regular filters. Therefore, this section will discuss how to design dual-mode filters using the higher-order modes of the SIW resonator.

Normally, degenerate modes are orthogonal to each other, with no energy coupling between them. According to reference [28], the condition for energy coupling between modes is provided as

$$\int \vec{H_1} \cdot \vec{H_2} dV \neq 0, \tag{1}$$

where vector H_1 and vector H_2 represent the magnetic field vectors of the two modes, respectively. The volume integrals are over entire effecting regions. The presence of a finite conductivity metal surface on the cavity wall causes losses, and this can be represented by the term in Equation (2)

$$\oint \vec{H_1} \cdot \vec{H_2} dS \neq 0. \tag{2}$$

The surface integrals are over entire effecting surface regions. There is energy transmission at the coupling gap, satisfying Equation (2), which can be treated as an equivalent lossy surface. Therefore, even if an ideal conductor is used in the actual fabrication, the coupling condition can still be met. This makes it possible to adjust the coupling gap to excite dual-mode modes. An analysis was conducted on a cavity with two coupling gaps, with coupling gap 1 serving as the input end, fed by a waveguide, and coupling gap 2 simulated as an impedance boundary to mimic actual loading conditions, as shown in Figure 1. From the simulation results, it can be concluded that when the input and output ends are co-axially arranged, it is impossible to achieve energy coupling between degenerate modes. When the input and output ends are not co-axially arranged, dual-mode excitation is related to the boundary conditions at the coupling gap. When the boundary condition at the coupling gap is purely reactive or open or short-circuited, the coupling gap experiences total reflection with no energy loss, so dual-mode excitation is not possible. From the perspective of field distribution, the electric field distribution in space is stable over time, forming a single-mode field with only amplitude variation, as shown in Figure 1. When the boundary condition at the coupling gap is set to a maximum impedance value, impedance-matched, or short-circuited, the electric field distribution near the boundary is strongest, and it approaches zero for short-circuited conditions. Capacitive and inductive boundary conditions also have different characteristics. When the boundary condition at the coupling gap is set to an appropriate impedance, dual-mode excitation can be achieved. From the perspective of field distribution, the dynamic effect of the electric field is rotational around the center over time, which indicates the superposition of two different field distributions. It can be regarded as the result of the superposition of the field excited by port 1 and the field excited by port 2. Thus, the conditions for exciting dual-mode modes are non-coaxial input and output and appropriate boundary impedance, both of which are essential. As the cavity has a selection function, the actual mode coupling situation also depends on the resonance frequency.

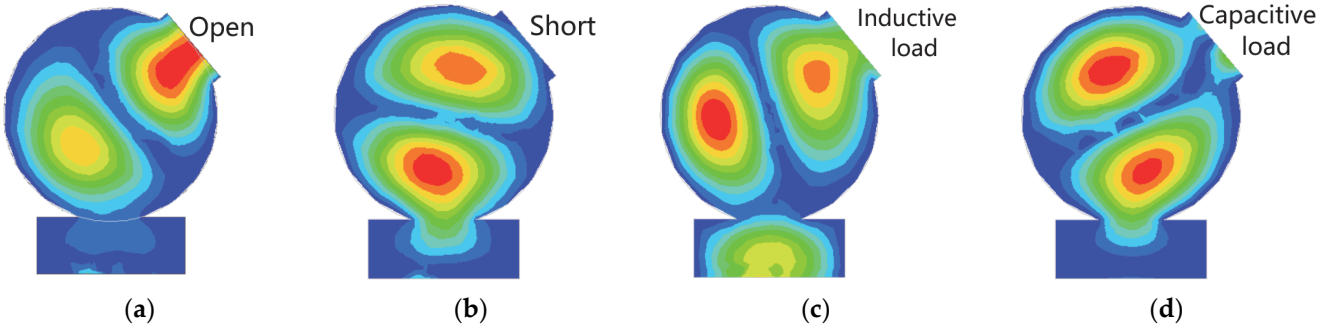

Figure 1. Electric field distribution under different reactance conditions with non-coaxial output: (**a**) open, (**b**) short, (**c**) inductive load, and (**d**) capacitive load. In the image, the red color represents the strongest electric field region, while the deep blue color represents the weakest electric field region.

Due to the symmetry in the structure of the circular cavity, the input and output end angles can be flexibly controlled to achieve mutual coupling between dual-mode filters. Therefore, a circular cavity is chosen for the design in this case.

2.2. Design Parameters Analysis

First, the excitation of individual cavity modes was studied. To better explain the design parameter, the configuration of the dual-mode filter with two cavities is illustrated in Figure 2. The whole filter is centrally symmetric. *R*1 represents the radius of circular cavity 1, which is the distance from the center of the cavity to the center of the ground vias. *alfa*1 denotes the angle between the centerline of the input port of circular cavity 1 and the centerline of the coupling port of cavity 1 and cavity 2. The vertex of the angle is the center of cavity 1, and the same vertex applies subsequently. *alfa*1_1 corresponds to the aperture size of the input port of cavity 1, which is the angle formed by the via centers of the two nearest grounded vias to the port and the center of cavity 1. These two ground vias are symmetrically distributed with the input port center line as the axis. *alfa*1_2 represents the aperture size of the coupling port of cavity 1 (coupling port of cavity 1 and cavity 2), which is the angle formed by the centers of the two nearest points to the coupling port and the center of the cavity. *depth*1 indicates the length to which the input coplanar waveguide (CPW) extends into the interior of the cavity. A positive value of *depth*1 indicates an inward extension into the cavity, while a negative value indicates the opposite direction. When the end of the slot coincides with the connecting line between the centers of the adjacent two grounded vias, it indicates that *depth*1 is 0 mm. *W_mcp* refers to the width of the microstrip line guided out, which corresponds to the width of the 50-ohm microstrip line in this design. Figure 3 shows the response of the dual modes of a single cavity under weak coupling conditions with varying *alpha*1. Weak coupling excitation was primarily intended to eliminate the influence of other factors, such as external coupling. It is evident that when the input and output are not co-axially symmetrically distributed, the coupling between degenerate modes increases with the increase in the input-output angle *alpha*1. When the relative bandwidth is below 6%, the *alpha* range can be selected between 110° to 130° based on the simulation results. From the field distribution plots of the low-frequency pole and high-frequency pole in Figure 4, it is evident that the two modes are orthogonal degenerate modes. Furthermore, a transmission zero point can be observed in the vicinity of the upper sideband, labeled as Z1. This creates a steep transition band, which is a characteristic feature of dual-mode filters. From the field distribution plot of the transmission zero point in Figure 5a, it can be seen that this field is a spatially stable single-mode field, with the output port located exactly at the wave node. Hence, it does not excite another mode from port 2. From a frequency perspective, this frequency point coincides with the resonance frequency of the cavity's first higher-order mode, TM110. Moreover, it can be observed from the subsequent study that the frequency of the transmission zero point is independent of the external coupling strength and the opening size of the coupling gap between the

cavities, as shown in Figure 5. Additionally, the impact of *alpha*1 on out-of-band suppression can be observed from Figure 5b. The second transmission zero point Z2 appears, and its position on the frequency axis increases with *alpha*1. The appearance of this pole was analyzed in the previous chapter. The frequency of this point coincides precisely with the position of the wave node, making the output energy zero. The position of this frequency point is solely determined by the angle *alpha*1 between the excitation end and the coupling end, irrespective of other parameters. The field distribution is shown in Figure 5b. By adjusting the position of Z2, the out-of-band suppression of the upper sideband can be significantly improved. If Z2 is located close to the passband, it improves the out-of-band suppression near the passband, making it suitable for filter designs requiring high near-end suppression. It is also possible to adjust Z2 to suppress the TM020 parasitic resonance closest to the TM010 mode, thereby achieving good out-of-band suppression at the far end of the high-frequency sideband. However, the trade-off for doing so is that the near-end suppression is relatively poor.

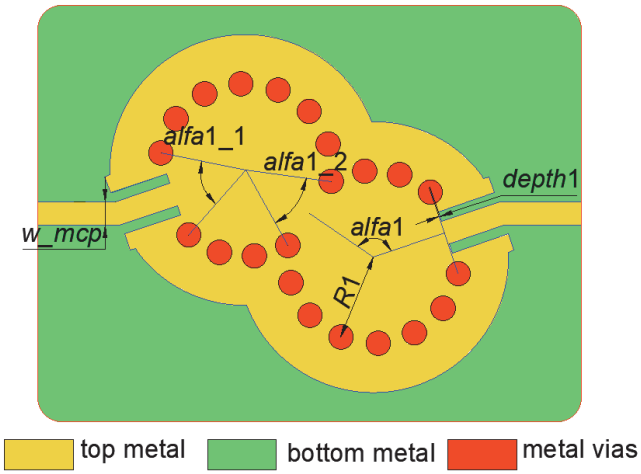

Figure 2. The layout of the dual-mode filter. *R*1 represents the radius of circular cavity 1. *alfa*1 denotes the angle between the input port center and coupling port center. *alfa*1_1 corresponds to the aperture angle size of the input port. *alfa*1_2 represents the aperture angle size of the coupling port. *depth1* indicates the inward extension of input CPW into the cavity.

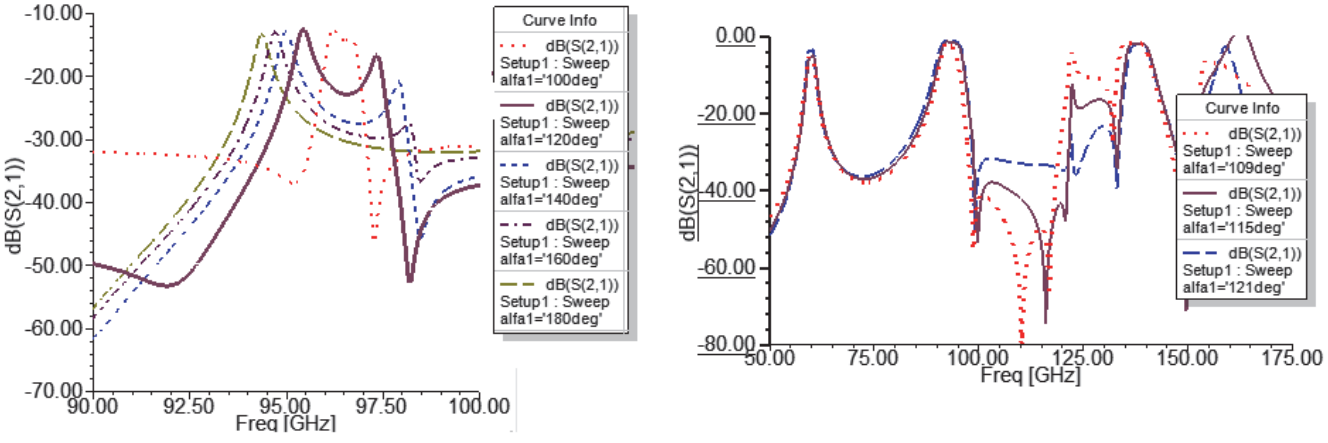

(**a**) (**b**)

Figure 3. The effect of alfa1 on S−parameters. (**a**) Effect within the passband under weak coupling excitation. (**b**) Effect on out-of-band suppression.

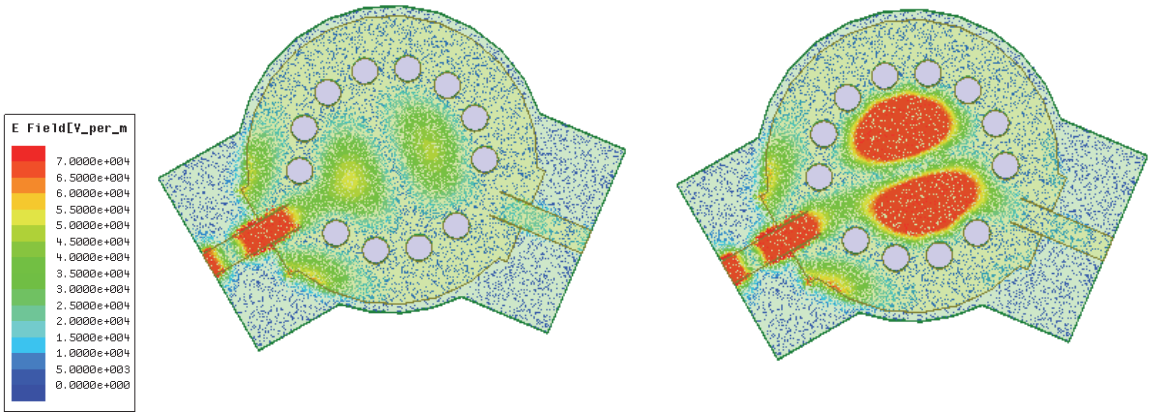

(**a**) (**b**)

Figure 4. Field structures of degenerate modes. (**a**) Low-frequency pole at 95.03 GHz. (**b**) High-frequency pole at 97.06 GHz.

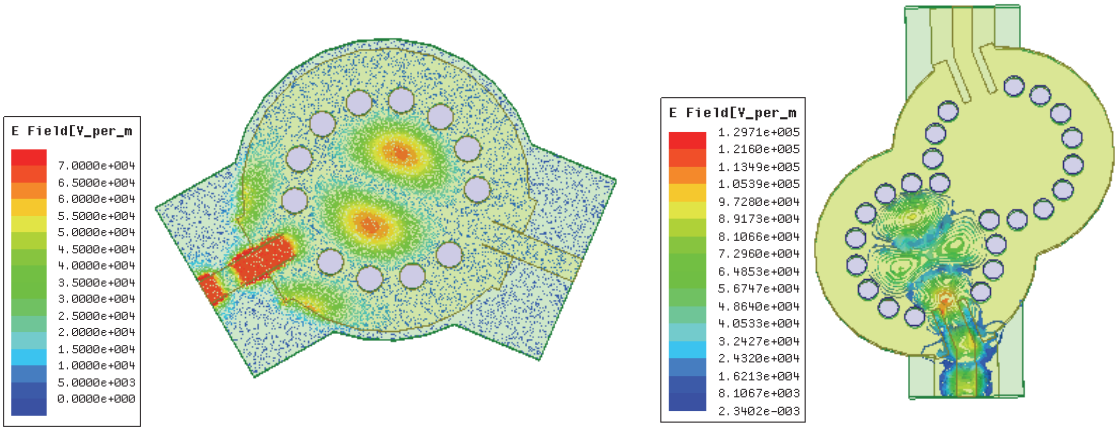

(**a**) (**b**)

Figure 5. Field structures at the positions of transmission zero points. (**a**) Low-frequency transmission zero point Z1. (**b**) High-frequency transmission zero point Z2.

For the design of in-band poles, the coupling between dual-mode cavities is complex, making it challenging to calculate precise coupling coefficient parameters. Therefore, a parameter sweeping method can be considered to observe the variation in each parameter's impact on the in-band poles and thereby improve the effectiveness of the final design. From Figure 6, it can be observed that $R1$ primarily influences the resonator's frequency and has almost no effect on the coupling strength. It only slightly affects the relative positions of the in-band poles. When $R1$ changes, the entire passband and stopband undergo vertical shifts, and the resonant frequency f_{nm} can be calculated using Equation (3) [29]

$$f_{nm} = \frac{p_{nm} \cdot c}{2\pi r \sqrt{\varepsilon_r \mu_r}}, \tag{3}$$

where P_{nm} is the mth root of the first kind Bessel function J_n, c is the speed of light in a vacuum, ε_r stands for relative permittivity, and μ_r stands for relative permeability, and the specific correction for the equivalent radius r of the cavity is as follows

$$r = R1 - dv/2 + 0.268(d_{vn})^{0.326}, \tag{4}$$

where $R1$ is the actual radius of the SIW cavity, dv is the aperture, and d_{vn} is the normalized aperture spacing.

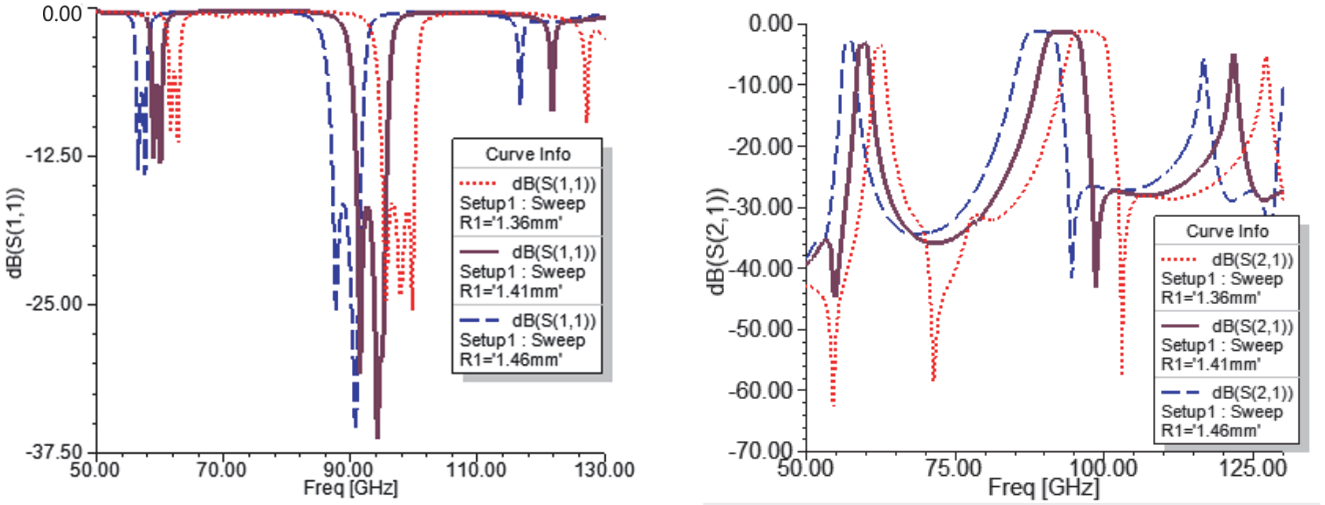

Figure 6. Influence of *R*1 on S−parameters.

Generally, for *R*1, the initial value should be chosen slightly higher than the passband frequency due to the coupling's effect on the resonant frequency.

The strength of external coupling is mainly controlled by the aperture angle *alpha*1_1 at the input end, as shown in Figure 7. When *alpha*1_1 is small, the positions of the poles are relatively far apart, resulting in poor standing wave levels. As *alpha*1_1 increases, the pole positions approach each other, leading to improved in-band standing wave performance. However, the rectangular coefficient and out-of-band suppressions slightly deteriorate. When *alpha*1_1 is at an appropriate level, the standing wave levels are better. Afterward, further increasing *alpha*1_1 brings the pole positions even closer, and excessive external coupling may cause pole merging, leading to deteriorated standing wave levels. As *alpha*1_1 increases, the resonant frequency decreases, causing the overall passband to shift downwards. From the perspective of out-of-band suppression, with the increase in *alpha*1_1, the external coupling becomes stronger, leading to a worse rectangular coefficient and out-of-band suppression.

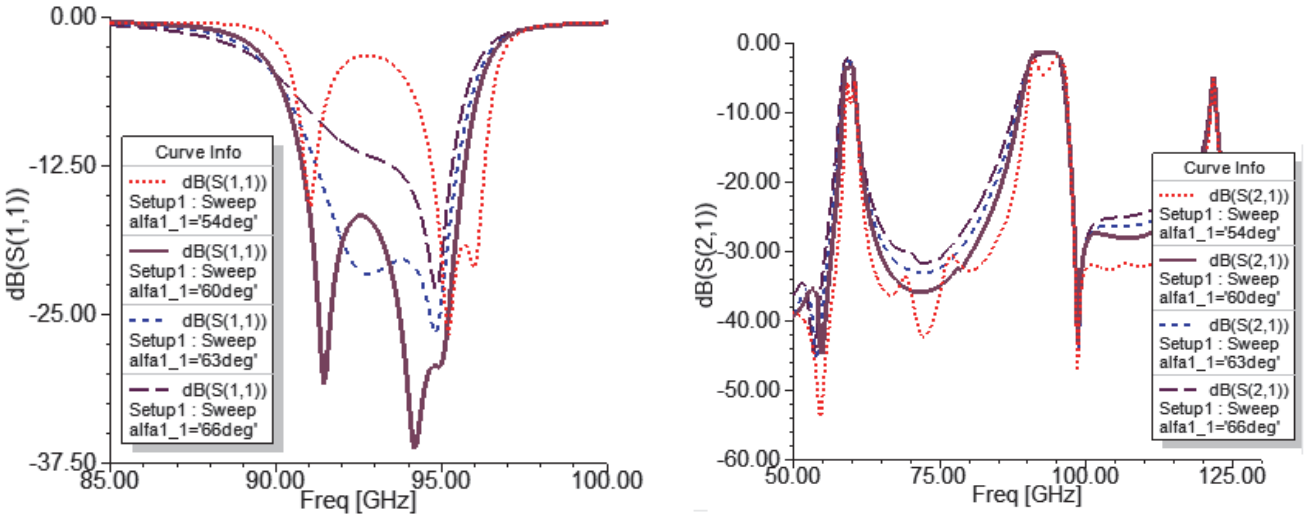

Figure 7. Influence of *alpha*1_1 on S−parameters.

The impact trend of the slot depth into the cavity (*depth*1) on out-of-band suppression and in-band standing waves is similar to that of the aperture *alpha*1_1, as shown in Figure 8. As *depth*1 increases, the rectangular coefficient and out-of-band suppressions slightly deteriorate. The difference lies in the effect on the relative positions of the poles. When *alpha*1_1 increases, the middle pole moves in the direction of higher frequency, while an

increase in *depth*1 results in the opposite effect. Therefore, by combining *alpha*1_1 and *depth*1 while ensuring appropriate external coupling, the relative positions of the poles can be adjusted to maintain a flat in-band standing wave. Additionally, *depth*1 has almost no impact on the resonant frequency of the resonator, which means it does not affect the center frequency of the passband, distinguishing it from *alpha*1_1, as analyzed in the previous chapter.

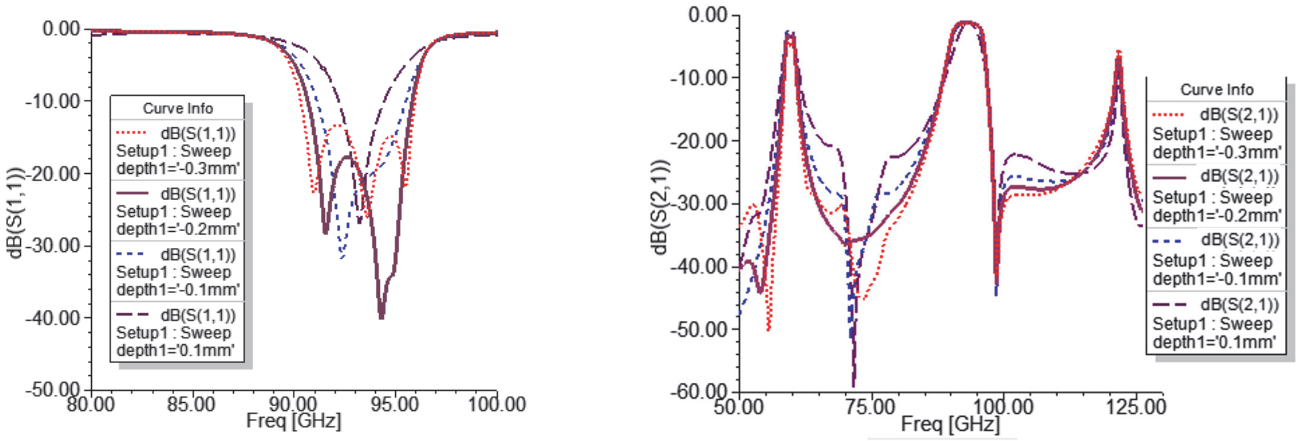

Figure 8. Influence of *depth*1 on S−parameters.

The coupling between cavities mainly depends on the coupling aperture angle (*alpha*1_2), as shown in Figure 9. When the coupling increases, the low-frequency in-band poles move downwards, while the frequency position of the high-frequency poles remains unchanged, resulting in an overall increase in bandwidth. The middle pole moves towards the direction of the high-frequency poles. With the increase in *alfa*1_2, the out-of-band suppression will degrade slightly.

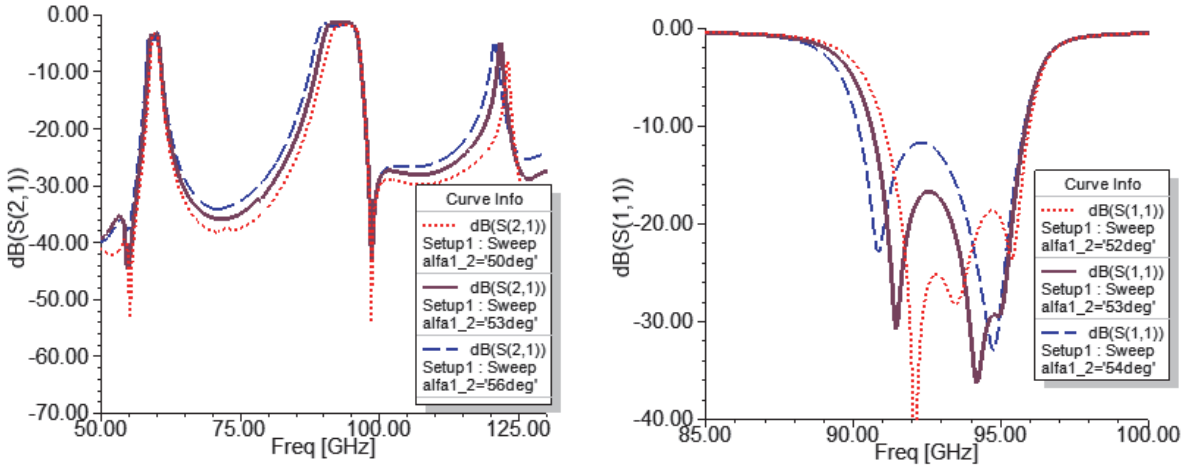

Figure 9. Influence of *alpha*1_2 on S−parameters.

3. Simulation Results and Experimental Analysis

Based on the design foundation described above, a W-band 4th-order dual-mode filter (Figure 2) with a passband from 91 to 95 GHz was designed. The substrate used was RT/DURIOD5880, with a thickness of 0.127 mm and a relative dielectric constant of ε_r = 2.2. The dimensions of the filter are listed in Table 1.

Table 1. Filter dimensions (unit: mm or deg).

	*alfa*1	*alfa*1_1	*alfa*1_2	*D*	*h*	*depth*1	*R*1	*w_mcp*
filter 1	127	60	53	0.4	0.508	−0.22	1.41	0.38

Due to the test instrument's port being a WR-10 waveguide, we designed a finline waveguide-to-microstrip transition structure with its length L_3 = 5 mm. Figure 10 illustrates a back-to-back finline waveguide-to-microstrip transition structure. Simulation results, as shown in Figure 11, indicate that this structure can cover a frequency range of approximately 80–110 GHz. The simulated insertion loss at 93 GHz is 0.75 dB. However, actual measurements usually show higher losses than simulated results, so the measured insertion loss for the back-to-back transition structure is expected to be greater than 0.75 dB. Ref. [18] tested a similar back-to-back transition structure in the W-band below 85 GHz and found measured insertion losses ranging from 0.94 to 1.4 dB in the frequency range of 75–85 GHz. Therefore, we conservatively estimate an insertion loss of 0.94 dB for the back-to-back transition structure in the following analysis.

Figure 10. A back-to-back finline waveguide-to-microstrip transition structure. The grey represents the WR-10 waveguide; the yellow corresponds to the front side metal; the blue is indicative of the back side metal; the green represents the Rogers 5880 substrate.

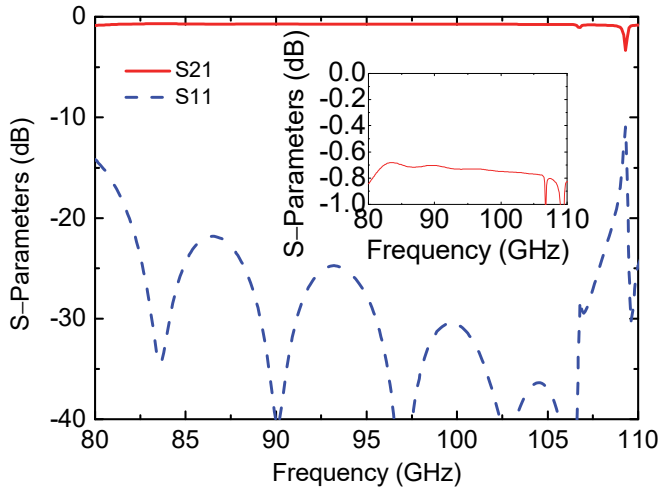

Figure 11. Simulated results for the structures in Figure 10.

Figure 12 presents the layout of the tested filter containing the waveguide-to-microstrip transition structure. The substrate is concealed to display the backside metal pattern more clearly. The blue color represents the front-side metal, and the green color represents the back-side metal. The core dimensions of the SIW filter are $L_0 \times W_0$, which is 6.8 mm × 5.95 mm. During the test, the layout shown in Figure 12 is placed inside the waveguide cavity manufactured from the waveguide cavity diagram in Figure 13. Figure 13a depicts the lower half of the cavity, where L_1 is the total length of the cavity, L_2 is the length of the filter, and the microstrip line extended from the SIW filter. Figure 13b illustrates the upper half of the cavity. Two small air cavities with a size of $L_4 \times W_4 \times h_2$ are left for the input and output CPW and microstrip line. For the convenience of fabrication, right angles are replaced with fillets of radius 0.3 mm. The distance between the two air cavities is denoted as L_5.

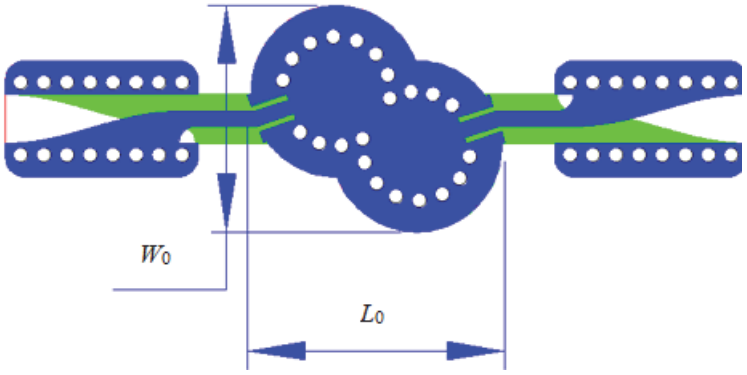

Figure 12. Layout of the proposed SIW filter with finline transitions.

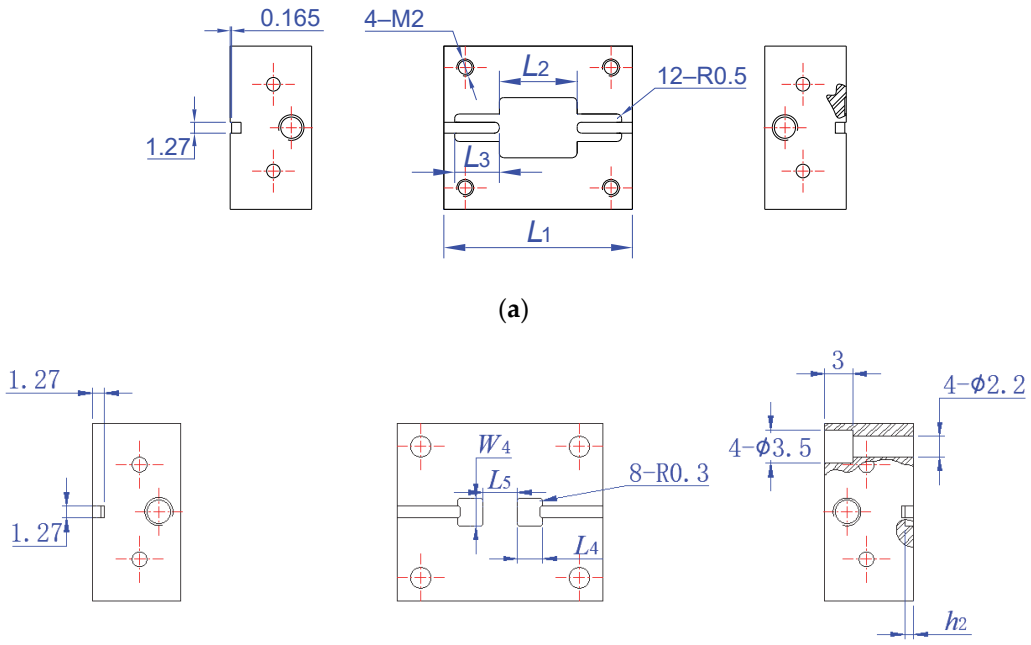

Figure 13. Waveguide cavity processing diagrams are used to load the structure shown in Figure 12. (**a**) The lower half of the cavity. (**b**) The upper half of the cavity. L_1 = 22 mm, L_2 = 9.07 mm, L_3 = 5.2 mm, W_4 = 2.92 mm, L_4 = 2.66 mm, and h_2 = 0.9 mm. The dimensional tolerance for the WR-10 waveguide fabrication is less than or equal to ±0.005 mm.

It is worth noting that the air cavity reserved above the microstrip line and coplanar waveguide will produce parasitic resonances. As the filter operates at high frequencies, these parasitic frequencies are likely to fall within the filter's passband. To address this issue, we separate the air cavity into two smaller ones, each with dimensions $W_4 \times L_4 \times h_2$. After verification, when W_4 = 2.92 mm, L_4 = 2.66 mm, and h_2 = 0.9 mm, our design requirements are met. Figure 14 shows a picture of the cavity loaded with the proposed filter and transitions. We conducted the testing using a network analyzer in the test setup shown in Figure 15. The measured results after de-embedding the transition structures are compared to the simulated results of the proposed filter in Figure 16.

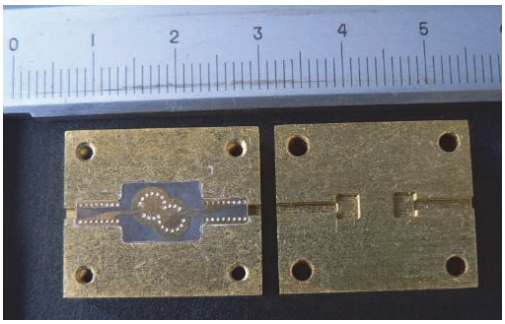

Figure 14. Photograph of the tested filter containing the transition structure used for testing.

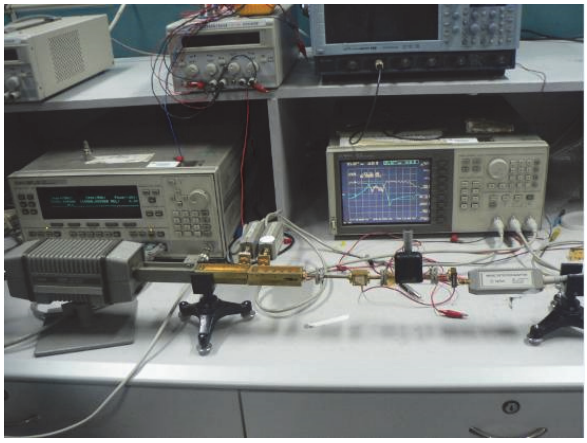

Figure 15. Measurement system and measurement environment.

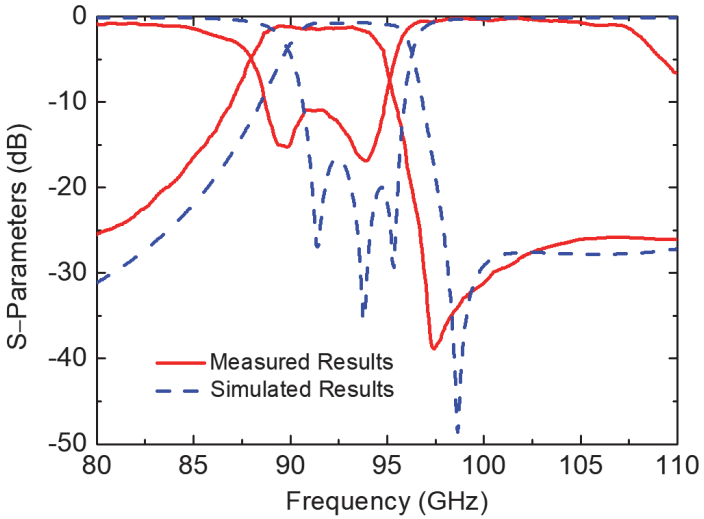

Figure 16. Simulated and measured results of the proposed filter after de-embedding.

From the simulation results, it can be observed that the insertion loss within the 90.6–95.6 GHz range is less than 1.5 dB. Specifically, within the 91–95 GHz sub-range, the insertion loss is less than 1 dB, and S11 within the passband is smaller than −15 dB. Additionally, there is a transmission zero in the high-frequency out-of-band region. Due to the short wavelength of the W-band, it is sensitive to dimensions, resulting in measured and simulated frequency deviations due to factors such as relatively larger processing errors in the PCB manufacturing process. Furthermore, the inclusion of non-ideal structures like waveguide-microstrip transitions in the test setup has a significant impact on the S11 curve, leading to substantial differences in the S11 curve.

Due to the impact of processing and assembly accuracy and roughness, the passband frequency is shifted downward. The test results after de-embedding the additional transition structures indicate an insertion loss below 2.06 dB from 88.8 GHz to 94 GHz, with a specific value of 1.36 dB at 92 GHz.

Table 2 presents a comparison between the planar or quasi-planar W-band filter designed in this study and those designed in other recent publications. The results show that this design exhibits lower losses and acceptable dimensions, particularly with significant manufacturing cost advantages, because both the MEMS process and chip fabrication process are much more expensive than the PCB process.

Table 2. Comparison with other W-band filters.

Ref.	f_0 (GHz)	Order	FBW(%)	IL at f_0 (dB)	Process	Type	Main Size (mm × mm)
[12]	100	4	5	1.2	SU8 MEMS	WG	12.2 × 2.54
[13]	94 G	4	8	0.9	MEMS	Gap WG	20 × 10
[14]	94.75	3	7.3	1.5	MEMS	Coaxial line	4.85 × 1.7
[15]	98.5	4	40	1.3	TSV	TLine	0.28 × 0.79
[17]	83	1	50.7	2.26	CMOS	WG	0.031 × 0.031
[18]	93	4	3.4	4.3	GaAs	WG	2.31 × 1.57
[21]	80	5	2.5	2.95	PCB	WG	8 × 5
[22]	89	5	22.5	1.97	Thin film MEMS	WG	2.6 × 2.6
[23]	92	3	3.26	1.8	Thin film MEMS	WG	5.8 × 5.8
This work	92	4	5.5	1.36	PCB	WG	6.8 × 5.95

Notes: "WG" in the table indicates planar or quasi-planar waveguide, while "TLine" stands for transmission line. The term "MEMS process" refers to the series of steps and techniques involved in the fabrication and manufacturing of micro-electro-mechanical systems (MEMS) devices. This process typically includes various microfabrication methods, such as photolithography, deposition, etching, and bonding, to create intricate structures and components on a microscale. "SU8" is a photoresist used for thick-film fabrication. "TSV" stands for "Through-Silicon Via". It refers to a vertical electrical connection that passes through a silicon wafer or substrate, allowing electrical signals to travel between different layers of a three-dimensional integrated circuit (3D-IC) stack.

In addition, a visible high-frequency out-of-band transmission zero has been implemented, which is used to enhance the steep roll-off characteristics in the high-frequency out-of-band region.

Regarding the frequency deviations caused by manufacturing, this is an inherent challenge at high frequencies due to the relatively lower precision of PCB manufacturing processes. On the one hand, considering the introduction of more precise manufacturing methods like laser etching can be explored. On the other hand, anticipating frequency deviations in the opposite direction in advance based on the characteristics of the manufacturing frequency shift can help counterbalance the effects of manufacturing-induced frequency shifts.

Regarding the disparities between simulation and measurement losses, we can address this by subsequently fabricating specific resonant structures and extracting more accurate metal roughness models from the measured loss data. This approach will result in simulations that closely approximate the manufacturing outcomes.

4. Conclusions

In this study, we have addressed the critical challenges associated with W-band filters in modern millimeter-wave communication and radar systems. These filters are indispensable components for various applications, including 5G/6G networks, automotive radars, and passive imaging. The increasing demand for higher data rates and more efficient wireless communication has spurred significant research and development efforts

in the realm of W-band filters over the past decade. Researchers have diligently explored diverse design techniques and advanced fabrication technologies in pursuit of improved performance and integration capabilities.

Our work presents a comprehensive solution to these challenges through the introduction of a PCB-based planar substrate-integrated waveguide (SIW) dual-mode cavity filter in W-band. By optimizing the filter's performance through a meticulous analysis of the dual-mode cavity coupling principle and design parameters, we aimed to provide an efficient and practical solution for W-band filtering requirements. Through a novel approach, we successfully realized and validated a low-loss SIW dual-mode filter in the W-band using commercially viable PCB processes. This approach not only offers substantial cost advantages over expensive advanced fabrication methods but also holds great promise due to its compatibility with direct integration into planar circuits.

The proposed filter exhibited an impressive low insertion loss of under 2.06 dB from 88.8 GHz to 94 GHz, with a specific value of 1.36 dB at 92 GHz, after accounting for the de-embedding of transition structures. Notably, we successfully introduced a high-frequency out-of-band transmission zero to enhance steep roll-off characteristics in the high-frequency out-of-band region. Comparison with recent publications showcased our designed W-band filter's remarkable attributes, including low losses and compact dimensions, all while maintaining considerable manufacturing cost advantages. By contributing to the ongoing advancements in the field of W-band filters, our research offers a perspective on achieving practical and efficient filtering solutions for modern millimeter-wave communication and radar systems.

In conclusion, the proposed planar SIW dual-mode cavity filter provides a valuable contribution to the field of W-band filters, offering an innovative solution to the challenges of integration, size, and cost. This work paves the way for further developments in low-cost and efficient W-band filtering solutions, catering to the evolving demands of millimeter-wave communication and radar systems.

Author Contributions: Methodology, X.H.; Validation, X.H.; Formal analysis, X.H.; Investigation, X.H.; Resources, X.H.; Data curation, X.H.; Writing—original draft, X.H.; Writing—review & editing, Z.L.; Funding acquisition, X.H.All authors have read and agreed to the published version of the manuscript.

Funding: This research was funded by [National Natural Science Foundation of China] grant number [62101193] And The APC was funded by [62101193].

Data Availability Statement: No new data were created or analyzed in this study. Data sharing is not applicable to this article.

Conflicts of Interest: The authors declare no conflict of interest.

References

1. Zhu, L.; Rossuck, I.W.; Payapulli, R.; Shin, S.H.; Lucyszyn, S. 3-D Printed *W*-Band Waveguide Twist with Integrated Filtering. *IEEE Microw. Wirel. Compon. Lett.* **2023**, *33*, 659–662. [CrossRef]
2. Bartlett, C.; Bornemann, J.; Höft, M. 3-D-printing and high-precision milling of *W*-band filter components with admittance inverter sequences. *IEEE Trans. Compon. Packag. Manuf. Technol.* **2021**, *11*, 2140–2147. [CrossRef]
3. Spain, W.; Chu, Y.; Crump, C.; Chahal, P. 3-D Printed *W*-band Substrate Integrated Waveguide Filter Using a Dam-and-Fill Process. In Proceedings of the 2022 IEEE International Symposium on Antennas and Propagation and USNC-URSI Radio Science Meeting (AP-S/URSI), Denver, CO, USA, 10–15 July 2022; pp. 1992–1993.
4. Salek, M.; Shang, X.; Roberts, R.C.; Lancaster, M.J.; Boettcher, F.; Weber, D.; Starke, T. *W*-band waveguide bandpass filters fabricated by micro laser sintering. *IEEE Trans. Circuits Syst. II Express Briefs* **2018**, *66*, 61–65. [CrossRef]
5. Shang, X.; Penchev, P.; Guo, C.; Lancaster, M.J.; Dimov, S.; Dong, Y.; Favre, M.; Billod, M.; De Rijk, E. *W*-band waveguide filters fabricated by laser micromachining and 3-D printing. *IEEE Trans. Microw. Theory Technol.* **2016**, *64*, 2572–2580. [CrossRef]
6. Xu, K.D.; Xia, S.; Guo, Y.J.; Cui, J.; Zhang, A.; Chen, Q. *W*-band *E*-plane waveguide bandpass filter based on meander ring resonator. *IEEE Microw. Wirel. Compon. Lett.* **2021**, *31*, 1267–1270. [CrossRef]
7. Huang, Z.; Jiang, Y.; Wu, W.; Liu, B.; Hu, W.; Yuan, N. *W*-band bandpass filter using rectangular microcoaxial structure. *IEEE Microw. Wirel. Compon. Lett.* **2021**, *31*, 957–960. [CrossRef]

8. Liu, Z.; Sharma, T.; Chappidi, C.R.; Venkatesh, S.; Yu, Y.; Sengupta, K. A 42–62 GHz transformer-based broadband mm-wave InP PA with second-harmonic waveform engineering and enhanced linearity. *IEEE Trans. Microw. Theory Technol.* **2020**, *69*, 756–773. [CrossRef]
9. Jiang, Y.; Huang, Z.; Liu, B.; Zhang, X.; Wang, C.; Wu, W.; Yuan, N. *W*-band *E*-plane waveguide filter using compact beeline resonator. *IEEE Microw. Wirel. Compon. Lett.* **2021**, *32*, 289–292. [CrossRef]
10. Liu, Z.; Sengupta, K. A 44–64-GHz mmWave broadband linear Doherty PA in silicon with quadrature hybrid combiner and non-foster impedance tuner. *IEEE J. Solid-State Circuits* **2022**, *57*, 2320–2335. [CrossRef]
11. Zhou, K.; Ding, J.Q.; Zhou, C.X.; Wu, W. *W*-Band Dual-Band Quasi-Elliptical Waveguide Filter with Flexibly Allocated Frequency and Bandwidth Ratios. *IEEE Microw. Wirel. Compon. Lett.* **2018**, *28*, 206–208. [CrossRef]
12. Leal-Sevillano, C.A.; Montejo-Garai, J.R.; Ke, M.; Lancaster, M.J.; Ruiz-Cruz, J.A.; Rebollar, J.M. A pseudo-elliptical response filter at *W*-band fabricated with thick SU-8 photo-resist technology. *IEEE Microw. Wirel. Compon. Lett.* **2012**, *22*, 105–107. [CrossRef]
13. Shi, Y.; Zhang, J.; Zhou, M.; Feng, W.; Cao, B.; Che, W. Miniaturized *W*-band gap waveguide bandpass filter using the MEMS technique for both waveguide and surface mounted packaging. *IEEE Trans. Circuits Syst. II Express Briefs* **2018**, *66*, 938–942. [CrossRef]
14. Song, S.; Yoo, C.S.; Seo, K.S. *W*-band bandpass filter using micromachined air-cavity resonator with current probes. *IEEE Microw. Wirel. Compon. Lett.* **2010**, *20*, 205–207. [CrossRef]
15. Wang, F.; Zhang, K.; Yin, X.; Yu, N.; Yang, Y. A Miniaturized Wideband SIR Interdigital Bandpass Filter with High Performance Based on TSV Technology for *W*-Band Application. *IEEE Trans. Compon. Packag. Manuf. Technol.* **2023**, *13*, 906–909. [CrossRef]
16. Chen, B.; Thapa, S.K.; Barakat, A.; Pokharel, R.K. A *W*-band compact substrate integrated waveguide bandpass filter with defected ground structure in CMOS technology. *IEEE Trans. Circuits Syst. II Express Briefs* **2021**, *69*, 889–893. [CrossRef]
17. Chen, B.; Thapa, S.K.; Barakat, A.; Pokharel, R.K. A *W*-Band 0.01 mm^2 Cavity Resonator Employing Slot-Loaded Shielded Folded Ridged Quarter-Mode in CMOS Technology. *IEEE Microw. Wireless Compon. Lett.* **2021**, *32*, 113–116. [CrossRef]
18. Xiao, Y.; Shan, P.; Zhao, Y.; Sun, H.; Yang, F. Design of a *W*-Band GaAs-Based SIW Chip Filter Using Higher Order Mode Resonances. *IEEE Microw. Wirel. Compon. Lett.* **2019**, *29*, 104–106. [CrossRef]
19. Chang, Y.C.; Lin, T.Y.; Wang, J.; Lin, S.G.; Hsieh, C.P.; Huang, Y.; Hsu, S.S.; Chang, D.C. A Miniature *W*-band Substrate-Integrated Waveguide Cavity Bandpass Filter Using GaAs-based IPD Technology. In Proceedings of the 2023 IEEE/MTT-S International Microwave Symposium—IMS 2023, San Diego, CA, USA, 11–16 June 2023; pp. 1109–1111.
20. Shi, Y.; Feng, W.; Wang, H.; Zheng, S.; Zhou, M.; Wu, Q. Compact planar *W*-band front-end module based on EBG packaging and LTCC circuits. *IEEE Trans. Circuits Syst. II Express Briefs* **2020**, *68*, 878–882. [CrossRef]
21. Hao, Z.C.; Ding, W.; Hong, W. Developing Low-Cost *W*-Band SIW Bandpass Filters Using the Commercially Available Printed-Circuit-Board Technology. *IEEE Trans. Microw. Theory Technol.* **2016**, *64*, 1775–1786. [CrossRef]
22. Huang, X.L.; Zhou, L.; Yuan, Y.; Qiu, L.F.; Mao, J.F. Quintuple-mode *W*-band packaged filter based on a modified quarter-mode substrate-integrated waveguide cavity. *IEEE Trans. Compon. Packag. Manuf. Technol.* **2019**, *9*, 2237–2247. [CrossRef]
23. Yang, L.; Yuan, Y.; Zhou, L. Low Loss *W*-Band Packaged Filtering Balun Based on a Modified Quarter-Mode Folded Substrate-Integrated Waveguide Cavity. *IEEE Access* **2022**, *10*, 64339–64347. [CrossRef]
24. Tan, S.; Yi, H.; Xiao, Y.; Chen, Z. A *W*-Band SIW Bandpass Filter with Controllable Transmission Zeros Using Perturbed Resonant Cavity. In Proceedings of the 2022 IEEE MTT-S International Microwave Workshop Series on Advanced Materials and Processes for RF and THz Applications (IMWS-AMP), Guangzhou, China, 27–29 November 2022; pp. 1–3.
25. Bartlett, C.; Bornemann, J.; Höft, M. Improved TM dual-mode filters with reduced fabrication complexity. *IEEE J. Microw.* **2022**, *3*, 60–69. [CrossRef]
26. Bartlett, C.; Höft, M. Dual-mode dual-band bandpass filter design utilising cylindrical TM-mode cavities. *Electron. Lett.* **2021**, *57*, 328–330. [CrossRef]
27. Bartlett, C.; Höft, M. *W*-band TE102-mode filter with doubly loaded *E*-plane and *H*-plane irises. *Electron. Lett.* **2021**, *57*, 190–192. [CrossRef]
28. Hong, J.-S. *Microstrip Filters for RF/Microwave Applications*, 2nd ed.; John Wiley & Sons, Inc.: Hoboken, NJ, USA, 2011; pp. 202–203.
29. Pozar David, M. *Microwave Engineering*, 4th ed.; Wiley: Hoboken, NJ, USA, 2012; pp. 289–290.